

Excitonic insulator emerging from semiconducting normal state in 1T-TiSe₂Jin Mo Bok* and Jungseok Hwang[✉]*Department of Physics, Sungkyunkwan University, Suwon 16419, Korea*Han-Yong Choi^{✉†}*Department of Physics, Sungkyunkwan University, Suwon 16419, Korea
and Asia Pacific Center for Theoretical Physics, Pohang 37673, Korea* (Received 15 November 2020; revised 29 March 2021; accepted 22 April 2021; published 5 May 2021)

A new state of matter, an excitonic insulator (EI) state, was predicted to emerge from Bose-Einstein condensation of electron-hole pairs. Some candidate materials were suggested but it has been elusive to confirm its existence. Recent works gave renewed support for the EI picture of the charge density wave (CDW) state below the critical temperature $T_c \approx 200$ K of 1T-TiSe₂. Yet, an important link to its establishment is to show that a majority fraction of the measured T_c indeed follows from the Coulomb interaction alone, while a quantitative match of the T_c may require assistance from the electron-lattice coupling. This will establish that the CDW is formed predominantly by the Coulomb interaction and help confirm the EI view for TiSe₂. Here, we provide such calculations by solving the exciton gap equation with material-specific electronic structures. We obtain, with no fitting parameters, $T_c \approx 135 \pm 27$ K for the normal state gap of $E_g \approx 74 \pm 15$ meV. It seems that the calculated T_c from Coulomb interaction gives a majority fraction of experimental T_c for recently determined values of E_g . The measured doping dependence of T_c was satisfactorily reproduced as well. Also in agreement with experiments is the same set of calculations of the photoemission spectroscopy and density of states. The semiconducting state above and EI below T_c together should give a coherent picture of 1T-TiSe₂.

DOI: [10.1103/PhysRevB.103.205108](https://doi.org/10.1103/PhysRevB.103.205108)**I. INTRODUCTION**

Coherent quantum states of excitons emerge out of a macroscopic number of electron-hole pairs bound by the Coulomb interaction as the band gap of semiconductors is reduced below the exciton binding energy [1]. They may Bose condense into a superfluid [2] or an insulating electronic crystal [3,4]. The exciton superfluid or excitonic insulator (EI) is a new state of matter which should have higher T_c scale than the traditional Bardeen-Cooper-Schrieffer (BCS) or Bose-Einstein condensation (BEC) states due to their light mass and the strong binding energy [2,5]. These states may provide a platform to investigate and utilize manifestations of macroscopic quantum phenomena. Exciton condensation in electronic double layers, where indirect excitons form out of photogenerated electrons and holes residing in spatially separated conducting layers, has been realized under strong magnetic field [6]. More recently the exciton superfluidity transport was observed in a quantized Hall regime in double bilayer graphenes at temperatures an order of magnitude higher than previously observed in GaAs double layers [7,8]. Despite these achievements there is a great need to identify materials in which an exciton condensate forms in equilibrium state without the applied field. TmSe_{0.45}Te_{0.55}, Ta₂NiSe₅,

and 1T-TiSe₂ have been investigated most intensely among candidate materials primarily because they have semiconducting and/or semimetallic electronic configuration with a small gap and/or overlap.

The 1T-TiSe₂ is a transition metal dichalcogenide semiconductor or semimetal of a layered structure with an indirect gap or overlap between the Se 4*p* hole band centered at the Γ point and the Ti 3*d* electron bands around the L (M for single-layer samples) points in the Brillouin zone (BZ) as shown in Fig. 1. An exciton, a bound state of an electron from the M_i band and a hole from the Γ band in Fig. 1(a), then has a nonzero net momentum and the inverse of the momentum sets a new length scale. Consequently, the exciton condensation is accompanied by a structural instability at the inverse momentum and makes a phase transition to CDW of $2a \times 2a \times 2c$ structure (where a and c are the lattice constants) below the critical temperature $T_c \approx 200$ K. Early transport and angle-resolved photoemission spectroscopy (ARPES) measurements found that TiSe₂ has a small band gap or overlap and low numbers of carriers which led to speculations of the CDW as an EI [9,10]. Also, the observation by high-resolution ARPES of a very flat valence-band dispersion near the Γ point and a large spectral weight transfer to backfolded bands in the CDW state seemed to be consistent with theoretical calculations on EI in TiSe₂ [11,12]. The nature of the resulting CDW, however, is subtle to distinguish from other mechanisms involving lattice degrees of freedom alone like the Peierls instability [13] or Jahn-Teller distortion [14]. An idea to differentiate them is to recall that the phonon

*Present address: Department of Physics, Pohang University of Science and Technology (POSTECH), Pohang 37673, Korea.

†Corresponding author: hychoi@skku.edu

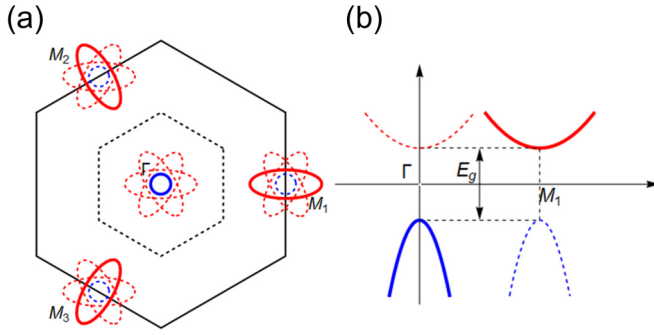


FIG. 1. (a) The first BZ of 1T-TiSe₂ exhibiting the hole band (blue) around the Γ and three electron bands (red) around M_i points. The BZ is reduced in the charge density wave (CDW) phase (black dashed line) and appear as the backfolded dispersions (red and blue dashed lines). (b) The energy dispersion of the hole and electron bands along the Γ - M_1 direction. E_g is the indirect bare gap between the electron and hole bands. The dashed lines are backfolded bands.

mode corresponding to the CDW structure becomes soft at T_c for electron-phonon coupled systems. Likewise, for a condensation of excitons of the momentum \mathbf{Q} there should appear a softening in the Coulomb interaction, that is, plasma frequency softening at the \mathbf{Q} as T approaches T_c . The recent momentum-resolved electron energy loss spectroscopy (EELS) experiments by Kogar *et al.* exactly observed this and gave a renewed support for the EI picture for 1T-TiSe₂ [15].

On the other hand, it should be noted that the excitonic and lattice instabilities should appear simultaneously as reported by Kogar *et al.* because they have the same spatial symmetry. It means that the origin of the CDW should be rephrased as a quantitative question as to which between the instabilities contributes more to open the CDW gap and to what extent. Then, a remaining theoretical step to a firm establishment of the EI in TiSe₂ is to check if a majority of the measured T_c indeed follows from the Coulomb interaction alone in material-specific calculations, while a quantitative match of the experimental T_c may need assistance from the electron-lattice coupling [16]. This will help establish that the CDW is formed predominantly by the Coulomb interaction, and confirm the EI view for TiSe₂. Here, we provide such calculations by solving a BCS-like exciton gap equation [3,11] with experimentally determined electronic structures.

The employed exciton gap equation as given by Eqs. (6) and (7) below is a mean-field approach which is reliable in the weak-coupling BCS regime. It also gives reliable T_c in the strong-coupling BEC regime as was discussed by Bronold and Fehske [17]. From the perspective of BCS-BEC crossover theory this may seem surprising because the mean-field theory does not account for preformed excitons above T_c on the semiconducting regime. However, the charge neutrality constraint in the present problem as given in Eq. (A9) leads to a cancellation of the leading-order corrections to the chemical potentials and forces T_c on the semiconducting side to coincide with the BEC transition temperatures for a noninteracting boson gas of excitons [17]. This justifies the employment of the gap equation for T_c determination in the semiconducting regime as well as the semimetallic one.

II. FORMULATION

The calculations of the exciton order parameter Δ and the critical temperature T_c presented here were performed by solving the exciton gap equation self-consistently by numerical iterations and finding the largest eigenvalue of the linearized gap equation. The gap equation is given by

$$\Delta_i(\mathbf{k}) = - \sum_{\mathbf{k}'} \int_{-\infty}^{\infty} d\omega A_{\Delta_i}(\mathbf{k}', \omega) f(\omega) V_s(\mathbf{k} - \mathbf{k}'), \quad (1)$$

where

$$\Delta_i(\mathbf{k}) = \langle a^\dagger(\mathbf{k}) b_i(\mathbf{k}) \rangle \quad (2)$$

($i = 1, 2, 3$) is the anomalous self-energy or the exciton order parameter formed between an electron from the M_i band and a hole from around Γ , and f is the Fermi-Dirac distribution function. A_{Δ} is the anomalous spectral function given by

$$\begin{aligned} A_{\Delta_i}(\mathbf{k}', \omega) &= -\frac{1}{\pi} \text{Im} G_{\Delta_i}(\mathbf{k}', \omega) \\ &= -\frac{1}{\pi} \text{Im} \frac{\Delta_i(\mathbf{k}')}{(\omega - \xi_{e,i})(\omega - \xi_h) - \Delta_i^2(\mathbf{k}') - B_i}, \end{aligned} \quad (3)$$

where ω should be understood as $\omega + i\delta$, with δ an infinitesimal. The $\xi_{e,i}$ and ξ_h are the dispersions for the i th electron band and hole band given by

$$\begin{aligned} \xi_{e,i}(\mathbf{k}) &= \varepsilon_{e,i}^0(\mathbf{k}) - \mu + E_g + \Sigma_{e,i}, \\ \xi_h(\mathbf{k}) &= \varepsilon_h^0(\mathbf{k}) - \mu + \Sigma_h, \end{aligned} \quad (4)$$

where E_g is the bare energy gap between the electron and hole bands and μ is the chemical potential. $\varepsilon_{e,i}^0$ and ε_h^0 are the bare dispersions of electron and hole bands, respectively, given by Eq. (A19), and $\Sigma_{e,i}$ and Σ_h are the corresponding self-energy given by Eq. (A17) in Appendix A.

B_i is the term arising from the coupling between the three electron bands given by

$$B_i(\omega, \mathbf{k}') = \sum_{j \neq i} \Delta_j^2(\mathbf{k}') \frac{\omega - \xi_{e,i}(\mathbf{k}')}{\omega - \xi_{e,j}(\mathbf{k}')}, \quad (5)$$

with i and j the electron band indices. A derivation of the exciton gap equation with the explicit electronic structure of TiSe₂ is outlined in Appendix A. A similar formulation was presented by Monney *et al.* [11].

For the kernel of the gap equation (1), we employed the two-dimensional (2D) Thomas-Fermi screened Coulomb interaction as the effective interaction between charge carriers in TiSe₂:

$$V_s(\mathbf{q}) = \frac{2\pi e^2}{\epsilon_\infty(q + q_s)}. \quad (6)$$

ϵ_∞ is the in-plane component of the background dielectric tensor of the three-dimensional (3D) TiSe₂ of layered structure and q_s is the screening wavenumber defined in Eq. (A6). Deduction of this form for TiSe₂ from the screened Coulomb interaction of layered structures, $V_s^{3D}(\mathbf{q}, q_z)$ of Eq. (B4), is discussed in Appendix B.

In the limit of $T \rightarrow T_c$, Δ_i , and B_i of Eq. (5) $\rightarrow 0$, and the exciton gap equation (1) is reduced to the linearized gap

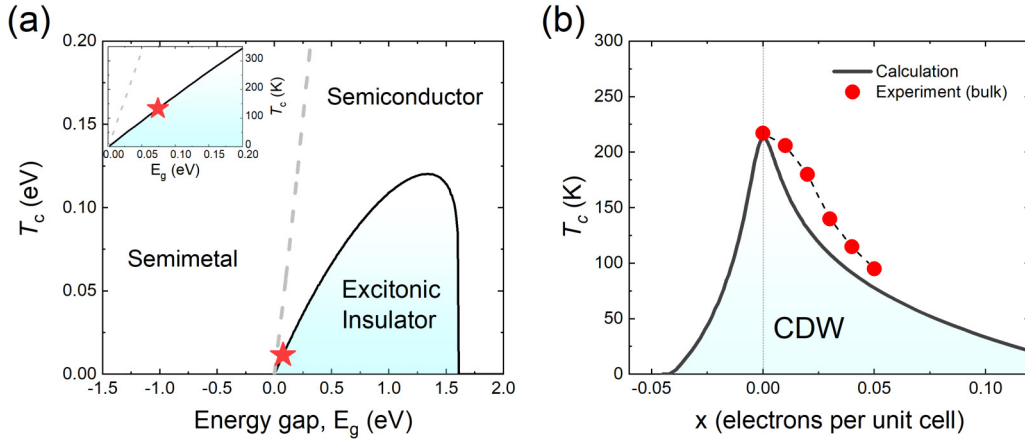


FIG. 2. (a) The EI phase diagram of $1T$ -TiSe₂ exhibiting T_c as a function of E_g for $\epsilon_\infty = 3.0$. The grey dashed line indicates the border between semimetal and semiconductor phases. The red star on the T_c curve shows the calculated $T_c = 135$ K corresponding to the recent measurement of $E_g = 74$ meV [18]. The inset shows an enlargement of the region around the red star. (b) The calculated doping dependence of T_c for $E_g = 0.12$ eV in comparison with experiments. The red circles represent measurements on pristine and Cu intercalated polycrystals [19].

equation [17]

$$\Delta(\mathbf{k}) = \int_{BZ} \frac{d\mathbf{k}'}{(2\pi)^2} V_s(\mathbf{k} - \mathbf{k}') \frac{f(\xi_h(\mathbf{k}')) - f(\xi_e(\mathbf{k}'))}{\xi_e(\mathbf{k}') - \xi_h(\mathbf{k}')} \Delta(\mathbf{k}'). \quad (7)$$

The order parameters Δ_i are related by a rotational symmetry and satisfy the same form of the gap equation as can be seen from Eq. (1). The solution of T_c is independent of the band index i and it was dropped out.

Equation (7) formally looks identical to the BCS gap equation. This similarity, however, holds only if the electron and hole have equal masses, and their dispersions are direct (negative) gap semimetals and satisfy $\xi_e(\mathbf{k}) = -\xi_h(-\mathbf{k})$ for one-electron and one-hole bands. In real materials these stringent requirements are necessarily not met and the celebrated Cooper logarithmic divergence is washed away. Consequently, the exciton instability is no longer a universal phenomenon in the BCS sense but becomes a number comparison problem of the exciton binding energy being larger than the band gap. Material-specific calculations are called for as discussed below.

III. EXCITON INSULATOR CRITICAL TEMPERATURE

It is crucial to determine the quantities q_s , Σ_i , and μ self-consistently as we did here by solving Eqs. (A6), (A9), and (A17) via numerical iterations for given temperature T , the background dielectric constant ϵ_∞ , and normal gap E_g . The self-consistency ensures the T_c from the exciton gap equation is reliable in the BEC as well as BCS regime as mentioned in the last paragraph in the Introduction section. With thus determined quantities, we write Eq. (7) in a matrix form by discretizing the wavevector \mathbf{k} within an irreducible BZ as

$$\Delta(\mathbf{k}_i) = \sum_j M(i, j) \Delta(\mathbf{k}_j). \quad (8)$$

We took the wavevector \mathbf{k} as an array of 48×48 k points within the hexagonal first BZ as explained in Appendix C. Equation (8) is just an eigenvalue problem with the eigenvalue set to 1. Above T_c all the eigenvalues are smaller than 1. Then,

T_c is given by the temperature where the largest eigenvalue of the matrix M of Eq. (8) becomes 1. This sets up a route to determine the EI critical temperature T_c microscopically with no fitting parameters.

T_c of $1T$ -TiSe₂ was calculated as the normal state gap E_g is varied taking the background dielectric constant $\epsilon_\infty = 3.0$. This gives the calculated T_c once the normal gap E_g is experimentally established. The determination of ϵ_∞ from the published experimental data and *ab initio* calculations is explained in Appendix D. The resulting phase diagram in the E_g - T plane is shown in Fig. 2(a). As can be seen from the figure, $T_c \approx 135 \pm 27$ K for the normal gap $E_g \approx 74 \pm 15$ meV (marked by the red star) recently determined by utilizing the photon-energy-dependent ARPES as we discuss about the normal state gap in the paragraph after next [18]. The measured CDW critical temperature is $T_c \approx 202$ K from the neutron diffraction measurement on bulk crystals [9], and on monolayers $T_c \approx 232$ K from ARPES [20] and ≈ 240 K from Raman experiments [21]. The calculated $T_c \approx 135 \pm 27$ K is smaller than the measured $T_c \approx 200$ K from bulk samples but is larger than half of it.

We also checked robustness of the results by calculating T_c from the 3D gap equation (B5) and Eq. (B4). The screened Coulomb interaction is weakened in three dimensions, which decreases T_c . On the other hand, for a fixed E_g , the minimum gap between Γ and L points in the 3D BZ, the k_z dispersion of the bands widens the average energy gap between the electron and hole bands, which should increase T_c around $E_g \approx 74$ meV as can be inferred from Fig. 2(a). This overcomes the decrease from the weakened Coulomb interaction and causes a net increase to $T_c \approx 150$ K for $E_g \approx 74$ meV as shown in Fig. 8 in Appendix C. Notwithstanding uncertainty in the normal state nature, it seems that the CDW formation in TiSe₂ is mainly by the Coulomb interaction. This should provide a much needed theoretical support for the EI picture of the CDW state of TiSe₂.

We wish to point out that the screened Coulomb interaction in monolayers of transition metal dichalcogenides is better described by the Rytova-Keldysh potential because of the dielectric contrast between a monolayer and surrounding

substrates or vacuum [22]. The parameters of the potential need to be determined before quantitative comparisons are made between experimental T_c and calculations for monolayers.

The EI phase in the low-temperature limit appears for $0 < E_g < E_X$, where E_X is the exciton binding energy. $E_X = 1.6$ eV for $\epsilon_\infty = 3.0$. It is given by

$$E_X \approx 2m_r c^2 \left(\frac{\alpha}{\epsilon_\infty} \right)^2 - \frac{\hbar^2 \overline{\Gamma M}^2}{2M}, \quad (9)$$

where $\alpha = e^2/\hbar c$, $\overline{\Gamma M}$ is the distance between Γ and M in the BZ, and m_r and M are, respectively, the reduced mass and total mass of an electron and a hole of an exciton, as discussed in Appendix C. The phase diagram for direct gap EI including its suppression in the semimetallic region was discussed by Bronold and Fehske [17]. The EI phase may be suppressed in the semimetallic region by the indirectness of the gap, the asymmetric mass ratio between electron and hole, or the number of conduction bands being larger than 1. Equation (7), which determines the EI phase diagram, is different from the superconducting gap equation as discussed above and is dependent on material-specific parameters including ϵ_∞ . Consequently, the EI phase diagrams presented here and in [17] look quite different from the presumed EI phase diagram [23] or from the BCS-BEC crossover of superconductors.

The normal state must be semiconducting for the EI to be a viable picture for the CDW phase of TiSe₂ as can be manifestly seen in Fig. 2(a). Yet, the nature of the normal state is still controversial. Some previous works reported semimetallic behaviors [9,14,20,24,25]. ARPES measurements showed that the electron band at the L point touches or crosses the Fermi level in the normal state and moves down to a lower energy as T is decreased [14,20]. It is consistent with metallic behavior of the T dependence of resistivity [9]. On the other hand, many spectroscopic and transport experiments reported a semiconducting normal state [18,26,27]. Watson *et al.*, utilizing the photon energy-dependent ARPES, presented results supporting the semiconducting normal state, $E_g \approx 74 \pm 15$ meV [18]. They also showed that the ‘‘passenger’’ states from the unhybridized Ti d conduction bands and the valence band around the A point remain decoupled from the CDW instability and provide the metallic behavior by accommodating extra charges from various extrinsic factors like crystal imperfections, Se vacancies, excess Ti, and residual iodine. Novello *et al.* also noticed that the semimetallic behavior in previous works actually came from crystal imperfections which can be controlled by new synthesis techniques, and that the imperfections are not related to the CDW phase formation [28]. Measurements on samples from the new synthesis techniques exhibited the anticipated insulating low-temperature behaviors [29,30].

To strengthen the arguments for the EI picture for TiSe₂, we consider the doping dependence of T_c by repeating the calculations as we vary the chemical potential. The doping dependence, $T_c(x)$, can be obtained by calculating T_c and the doping concentration x as a function of the chemical potential μ . Because the doping increases the screening wavenumber q_s , the Coulomb binding energy is weakened, and $T_c(x)$ should be a decreasing function of x . Figure 2(b) shows that the

calculated $T_c(x)$ (black solid line) is in good agreement with the electron doping experiments. The T_c suppression rate by hole doping is steeper than the electron doping as might be expected because the conduction band has higher density of states (DOS). The $T_c(x)$ result also suggests that pristine TiSe₂ to exhibit intrinsic behavior might be prepared by hole or electron doping such that the samples have a maximum T_c with doping.

The pressure dependence of T_c may be considered similarly. Pressure induces more overlap between the electron and hole bands and a decrease of the gap. This leads to more screening and weakened interaction, which suppresses the T_c within the EI picture. This behavior was indeed observed experimentally [24].

IV. SPECTROSCOPIC FEATURES

We now turn to the spectroscopic features of the ARPES and DOS below T_c . In the low-temperature regime deep in the CDW state, the full gap equation of Eq. (1) must be solved self-consistently to obtain $\Delta_i(\mathbf{k})$. All three gap order parameters $\Delta_i(\mathbf{k})$ are coupled in the full gap equation unlike the linearized one, and they are calculated simultaneously. We assumed they are real for simplicity with no consideration of the possible chirality of the order parameter phase. The sum over \mathbf{k}' in Eq. (1) was performed using the fast Fourier transform with a 48×48 k point mesh within the hexagonal first BZ as is explained in Appendix E. The indirectness of the gap was properly taken into consideration in this process. The computed $\Delta_i(\mathbf{k})$ is shown in the first BZ in Fig. 3.

With the determined $\Delta_i(\mathbf{k})$ as shown in Fig. 3, the spectral functions of the hole and electron bands which ARPES measure are then given as below:

$$A_{e,i}(\mathbf{k}, \omega) = -\frac{1}{\pi} \text{Im} \frac{\omega - \xi'_h - B_i / (\omega - \xi_{e,i})}{(\omega - \xi_{e,i})(\omega - \xi'_h) - \Delta_i^2(\mathbf{k}) - B_i},$$

$$A_h(\mathbf{k}, \omega) = -\frac{1}{\pi} \text{Im} \frac{\omega - \xi'_{e,3}}{(\omega - \xi'_{e,3})(\omega - \xi_h) - \Delta_3^2(\mathbf{k}) - B'_3}, \quad (10)$$

where ξ' are the backfolded dispersions of the corresponding electron and hole bands. The DOS is obtained by summing the spectral function $A(\mathbf{k}, \omega)$ over the wavevector \mathbf{k} by

$$D(\omega) = \sum_{\mathbf{k}} \left[\sum_{i=1,2,3} A_{e,i}(\mathbf{k}, \omega) + A_h(\mathbf{k}, \omega) \right]. \quad (11)$$

The renormalized dispersions in the EI states show up in high intensity as shown in Figs. 4(a) and 4(b). The calculated spectra are in good agreement with Monney *et al.* [11]. The most significant distinction is that the exciton order parameter with the full momentum dependence was calculated self-consistently from the screened Coulomb interaction in the present work. The conduction and hole dispersions are hybridized in the EI state. Around, say, the M_1 point, the $\xi_{e,1}$ out of the triplet conduction bands and the hole dispersion ξ_h are coupled and shifted up and down, respectively, and show up with high intensity as shown in Figs. 4(a) and 4(b). Their backfolded bands also clearly show up. The renormalized conduction band is shift up from $\xi_{e,1}$ and shows a flat disper-

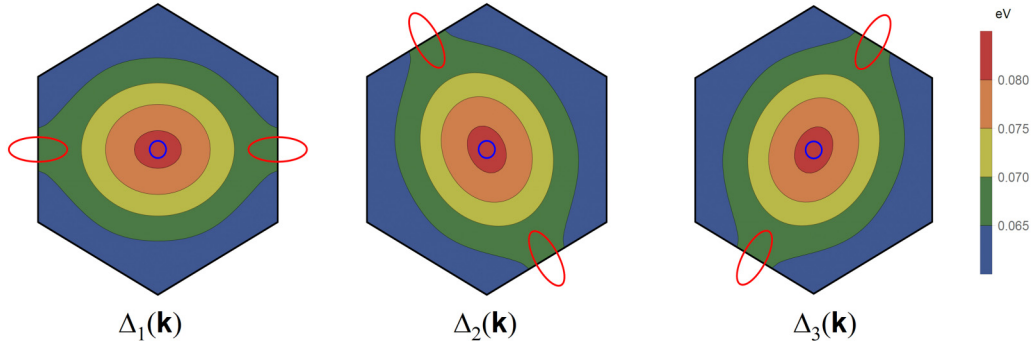


FIG. 3. The momentum dependence of the computed order parameter $\Delta_i(\mathbf{k})$ within the first BZ. The blue and red lines are the hole and electron bands, respectively. $\Delta_i(\mathbf{k})$ takes the largest value at the BZ center and is elongated along Γ - M_i direction.

sion around the M_1 point. The other two electron dispersions remain little affected. Consequently, they overlap with the bare dispersions (the orange dashed lines) and their backfoldings have a vanishing intensity.

Some of these features may be better studied by the scanning tunneling spectroscopy (STS) and scanning tunneling microscopy (STM) experiments because ARPES cannot probe the unoccupied states. The tunneling conductance (dI/dV) is proportional to the DOS given by Eq. (11). The calculated DOS above and below T_c are shown in Fig. 4(c). The coherence peaks become split due to the momentum dependence of the exciton order parameter: two-step-like structure in the negative bias (green arrows) and two-peak structure in the positive bias (black arrows) regime. Interesting features may be revealed more clearly in the normalized conductance of $(dI/dV)_{CDW}/(dI/dV)_{normal}$ as shown in Fig. 4(d). Most important is the clear zero-bias peak of the width of the normal gap as marked by the red arrow. This is because the normal state is semiconducting with the gap E_g and the

EI has a bigger gap of $\sqrt{E_g^2 + 3(2\Delta_\Gamma)^2}$ or $\sqrt{E_g^2 + 3(2\Delta_M)^2}$. Systematic analysis of DOS is not available in the literature. But, the recent STS experiments of Kolekar *et al.* [27] (reproduced in Appendix E) do exhibit the anticipated zero-bias peak, which is consistent with the semiconducting normal state. High-resolution STS data in a wide bias range will be informative.

V. SUMMARY AND CONCLUDING REMARKS

We presented in this paper a theoretical investigation of the view that the charge density wave below $T_c \approx 200$ K is an excitonic insulator phase in $1T$ -TiSe₂. The idea was to check if the calculated T_c from the Coulomb interaction alone accounts for a majority fraction of the experimental T_c . If so, it implies that the observed CDW is predominantly formed by the Coulomb interaction and that the CDW is an EI phase. Two crucial physical parameters for a quantitative determination of T_c were the background dielectric constant

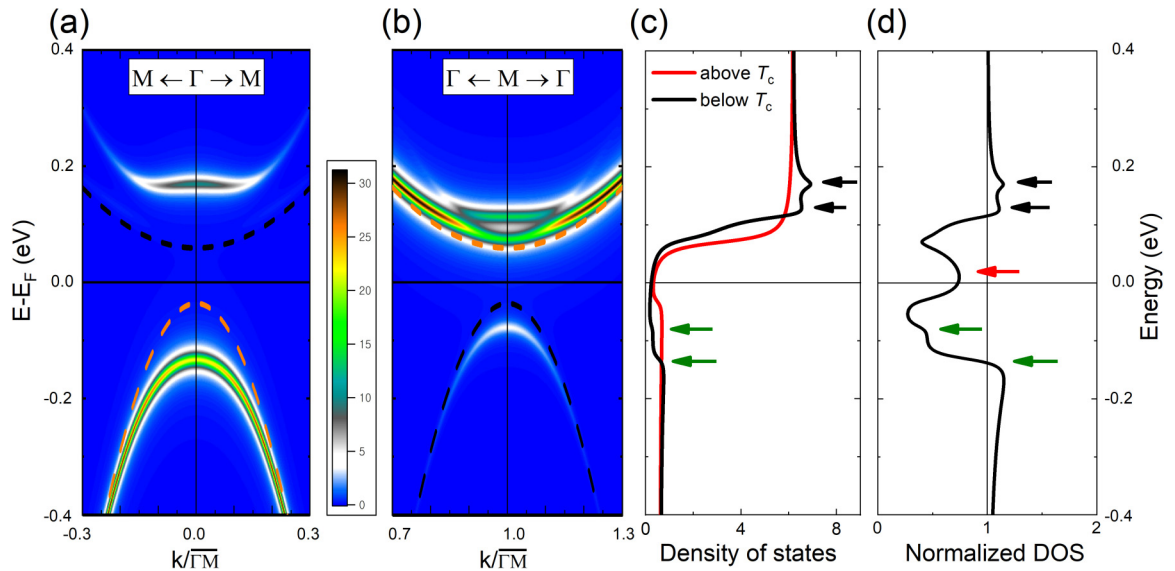


FIG. 4. (a, b) The calculated spectral function around Γ and M points. The orange dashed lines represent the (a) hole and (b) electron dispersions in the normal phase and the black dashed lines show their backfolded ones. The high-intensity curves near the orange lines are the main dispersions in the EI state. (c) DOS in EI (black line) and normal (red) states. The black and green arrows indicate the coherence peaks due to flat dispersions of spectral function. These peaks are split because of the momentum dependence of $\Delta_i(\mathbf{k})$. (d) The normalized DOS, where the zero-bias peak (marked by the red arrow) shows up because of the normal state gap.

ϵ_∞ and the normal state gap E_g . We determined $\epsilon_\infty \approx 3.0$ by combining the published reflectance spectrum and EELS measurements up to 30 eV. If we take $E_g \approx 74 \pm 15$ meV as a representative value, we obtained $T_c \approx 135 \pm 27$ K. This accounts for majority fraction of the measured $T_c \approx 200$ K from bulk crystals, while a quantitative match of the measured T_c may need assistance from other interactions like the electron-lattice coupling and the Jahn-Teller effect. It seems that the EI is a convincing view of the CDW state of $1T$ -TiSe₂.

The EI view was furthermore reinforced by calculating the doping dependence of the critical temperature $T_c(x)$ and the spectroscopic features in the low-temperature limit. These calculations were done with the same set of parameters as the T_c calculations of undoped samples and were in agreement with experimental observations. We note again that the EI phase emerges only out of a semiconducting normal state (positive E_g). The semiconducting state above T_c and EI below together should give a coherent picture of $1T$ -TiSe₂.

The semimetallic or semiconducting normal state behavior turns out to be a crucial facet of underlying physics which may help uncover nature of CDWs of disparate mechanisms. The underlying physics of the Peierls instability or Jahn-Teller distortion is to lift degeneracy or to reduce the DOS at the Fermi level by a CDW distortion to lower the free energy. This implies that a metallic DOS at the Fermi level is favored for the Peierls instability or Jahn-Teller distortion to be operative. On the other hand, the excitons may condense in the metallic or insulating states in, respectively, BCS or BEC regimes. Therefore, a CDW out of a semiconducting normal state is expected to be of an excitonic nature. This physical anticipation is indeed borne out to be the case for TiSe₂ by detailed material-specific calculations in this paper. We anticipate our approach to be applied to a wider class of problems and materials where the exciton condensation is yet to be explored.

ACKNOWLEDGMENTS

We thank Sadhu Kolekar and Matthias Batzill for providing us with the experimental STS data, and Matthew Watson, Claude Monney, Chandra Varma, and Yunkyu Bang for discussion and comments on the manuscript. The work was supported by the Samsung Science and Technology Foundation (SSTF) through Grant No. SSTF-BA1502-06 and by National Research Foundation (NRF) of Korea through Grants No. NRF-2018R1D1A1B07043997 (H.Y.C.), No. NRF-2019R1I1A1A01057393 (J.M.B.), and No. NRF-2019R1A6A1007307912 (J.H.).

APPENDIX A: FORMULATION OF THE EXCITON GAP EQUATION FOR $1T$ -TiSe₂

To describe the excitonic insulator state of $1T$ -TiSe₂, we considered three Ti $3d$ -derived electron bands around M_i and a Se $4p$ -derived hole band around Γ in the BZ with statically screened Coulomb interaction. The Hamiltonian is written as

$$H = H_0 + W, \quad (\text{A1})$$

$$H_0 = \sum_{\mathbf{k}} \epsilon_h(\mathbf{k}) a^\dagger(\mathbf{k}) a(\mathbf{k}) + \sum_{\mathbf{k}, i} \epsilon_{e,i}(\mathbf{k}) b_i^\dagger(\mathbf{k}) b_i(\mathbf{k}), \quad (\text{A2})$$

$$W = \frac{1}{2} \sum_{\mathbf{q}, i} \rho_a(\mathbf{q}) V_s(\mathbf{q}) \rho_{b,i}(-\mathbf{q}), \quad (\text{A3})$$

where the density operators are

$$\rho_a(\mathbf{q}) = \sum_{\mathbf{k}} a^\dagger(\mathbf{k} + \mathbf{q}) a(\mathbf{k}), \quad (\text{A4})$$

$$\rho_{b,i}(\mathbf{q}) = \sum_{\mathbf{k}} b_i^\dagger(\mathbf{k} + \mathbf{q}) b_i(\mathbf{k}). \quad (\text{A5})$$

Here ϵ_h and $\epsilon_{e,i}$ are the hole and electron dispersions and i is the electron band index. $V_s(\mathbf{q})$ is the Thomas-Fermi screened Coulomb interaction in two dimensions given in Eq. (6) in the main text. q_s is the screening wavenumber given by

$$q_s = \frac{2\pi e^2}{\epsilon_\infty} \frac{\partial n}{\partial \mu}, \quad (\text{A6})$$

where μ is the chemical potential and n is the sum of the densities of three electron bands and one hole band,

$$n(\mu, T) = \sum_{i=1,2,3} n_{e,i}(\mu, T) + n_h(\mu, T), \quad (\text{A7})$$

with

$$n_{e,i}(\mu, T) = 2 \int_{BZ} \frac{d\mathbf{k}}{(2\pi)^2} f(\xi_{e,i}),$$

$$n_h(\mu, T) = 2 \int_{BZ} \frac{d\mathbf{k}}{(2\pi)^2} f(-\xi_h), \quad (\text{A8})$$

where the factor of 2 is due to the spin degeneracy.

The charge neutrality condition is

$$\sum_{i=1,2,3} n_{e,i}(\mu, T) = n_h(\mu, T). \quad (\text{A9})$$

Deviations from the charge neutrality are represented by the doping concentration x which can be calculated by varying the chemical potential μ . x is given by

$$x(\mu, T) = \sum_{i=1,2,3} n_{e,i}(\mu, T) - n_h(\mu, T), \quad (\text{A10})$$

for given temperature T and μ .

We employ the four-component operator $\Psi_{\mathbf{k}}$ in Nambu notation:

$$\Psi_{\mathbf{k}}^\dagger = (b_1^\dagger(\mathbf{k}), b_2^\dagger(\mathbf{k}), b_3^\dagger(\mathbf{k}), a^\dagger(\mathbf{k})), \quad \Psi_{\mathbf{k}} = \begin{pmatrix} b_1(\mathbf{k}) \\ b_2(\mathbf{k}) \\ b_3(\mathbf{k}) \\ a(\mathbf{k}) \end{pmatrix}. \quad (\text{A11})$$

The 4×4 matrix renormalized Green's function \hat{G} is defined as

$$\hat{G}(\mathbf{k}, \tau) = -\langle T_\tau \Psi_{\mathbf{k}}(\tau) \Psi_{\mathbf{k}}^\dagger(0) \rangle, \quad (\text{A12})$$

with the bare Green's function \hat{G}_0 and the self-energy $\hat{\Sigma}$ given as

$$\hat{G}_0^{-1}(\mathbf{k}, ip) = ip - \begin{pmatrix} \varepsilon_{e,1}(\mathbf{k}) & 0 & 0 & 0 \\ 0 & \varepsilon_{e,2}(\mathbf{k}) & 0 & 0 \\ 0 & 0 & \varepsilon_{e,3}(\mathbf{k}) & 0 \\ 0 & 0 & 0 & \varepsilon_h(\mathbf{k}) \end{pmatrix}, \quad (\text{A13})$$

$$\hat{\Sigma}(\mathbf{k}, ip) = \begin{pmatrix} \Sigma_{e,1}(\mathbf{k}, ip) & 0 & 0 & \Delta_1(\mathbf{k}, ip) \\ 0 & \Sigma_{e,2}(\mathbf{k}, ip) & 0 & \Delta_2(\mathbf{k}, ip) \\ 0 & 0 & \Sigma_{e,3}(\mathbf{k}, ip) & \Delta_3(\mathbf{k}, ip) \\ \Delta_1(\mathbf{k}, ip) & \Delta_2(\mathbf{k}, ip) & \Delta_3(\mathbf{k}, ip) & \Sigma_h(\mathbf{k}, ip) \end{pmatrix}. \quad (\text{A14})$$

The renormalized Green's function is given by Dyson's equation as

$$\hat{G}^{-1}(\mathbf{k}, ip) = \hat{G}_0^{-1}(\mathbf{k}, ip) - \hat{\Sigma}(\mathbf{k}, ip) = \begin{pmatrix} ip - \xi_{e,1}(\mathbf{k}) & 0 & 0 & -\Delta_1(\mathbf{k}, ip) \\ 0 & ip - \xi_{e,2}(\mathbf{k}) & 0 & -\Delta_2(\mathbf{k}, ip) \\ 0 & 0 & ip - \xi_{e,3}(\mathbf{k}) & -\Delta_3(\mathbf{k}, ip) \\ -\Delta_1(\mathbf{k}, ip) & -\Delta_2(\mathbf{k}, ip) & -\Delta_3(\mathbf{k}, ip) & ip - \xi_h(\mathbf{k}) \end{pmatrix} \quad (\text{A15})$$

in the Matsubara frequency.

The normal state dispersions are

$$\xi_{e,i}(\mathbf{k}) = \varepsilon_{e,i}^0(\mathbf{k}) - \mu + E_g + \Sigma_{e,i}, \quad \xi_h(\mathbf{k}) = \varepsilon_h^0(\mathbf{k}) - \mu + \Sigma_h, \quad (\text{A16})$$

as given previously in the main text. The diagonal self-energies $\Sigma_{e,i}$ and Σ_h are given by

$$\Sigma_{e,i} = -2 \sum_{\mathbf{k}} V_s(\mathbf{k}) f(\xi_i(\mathbf{k})), \quad \Sigma_h = 2 \sum_{\mathbf{k}} V_s(\mathbf{k}) f(-\xi_h(\mathbf{k})). \quad (\text{A17})$$

Σ and q_s were also determined self-consistently by keeping the charge neutrality [17]. The renormalized band gap is

$$\bar{E}_g = E_g + \Sigma_e - \Sigma_h. \quad (\text{A18})$$

The 2D bare dispersions within the hexagonal first BZ were taken as

$$\begin{aligned} \varepsilon_{e,1}^0(k_x, k_y) &= \frac{\hbar^2}{2m_{e,l}} (k_x - \overline{\Gamma M})^2 + \frac{\hbar^2}{2m_{e,s}} k_y^2, \\ \varepsilon_{e,2}^0(k_x, k_y) &= \frac{\hbar^2}{2m_{e,l}} \left(\frac{1}{2} \left(k_x + \frac{\overline{\Gamma M}}{2} \right) - \frac{\sqrt{3}}{2} \left(k_y - \frac{\sqrt{3}}{2} \overline{\Gamma M} \right) \right)^2 + \frac{\hbar^2}{2m_{e,s}} \left(\frac{\sqrt{3}}{2} \left(k_x + \frac{\overline{\Gamma M}}{2} \right) + \frac{1}{2} \left(k_y - \frac{\sqrt{3}}{2} \overline{\Gamma M} \right) \right)^2, \\ \varepsilon_{e,3}^0(k_x, k_y) &= \frac{\hbar^2}{2m_{e,l}} \left(\frac{1}{2} \left(k_x + \frac{\overline{\Gamma M}}{2} \right) + \frac{\sqrt{3}}{2} \left(k_y + \frac{\sqrt{3}}{2} \overline{\Gamma M} \right) \right)^2 + \frac{\hbar^2}{2m_{e,s}} \left(\frac{\sqrt{3}}{2} \left(k_x + \frac{\overline{\Gamma M}}{2} \right) - \frac{1}{2} \left(k_y + \frac{\sqrt{3}}{2} \overline{\Gamma M} \right) \right)^2, \\ \varepsilon_h^0(k_x, k_y) &= -\frac{\hbar^2}{2m_h} (k_x^2 + k_y^2), \end{aligned} \quad (\text{A19})$$

for the three elliptic electron bands at M_i points and a hole band at Γ , where $\overline{\Gamma M}$ is the distance between Γ and M points in the reciprocal space. We took

$$\begin{aligned} m_{e,l} &= 3.46 \times \text{free electron mass}, \\ m_{e,s} &= 1.38 \times \text{free electron mass}, \\ m_h &= 0.63 \times \text{free electron mass}, \end{aligned} \quad (\text{A20})$$

for the effective masses of the conduction and hole bands [20,31].

APPENDIX B: THE SCREENED COULOMB INTERACTION FOR TiSe₂ OF LAYERED STRUCTURE

We calculated the critical temperature T_c of the exciton condensation by solving the linearized gap equation (7). The inputs are the material-specific electronic structure and the effective screened Coulomb interaction V_s . Let us first consider V_s .

Recall that the solution to the anisotropic Poisson equation with the in-plane and out-of-plane dielectric constants ϵ_{\parallel} and ϵ_{\perp} is given as

$$V(\mathbf{r}, z) = \frac{e}{\sqrt{\epsilon_{\parallel}\epsilon_{\perp}}} \frac{1}{\sqrt{r^2 + \frac{\epsilon_{\parallel}}{\epsilon_{\perp}} z^2}}, \quad (\text{B1})$$

as may be verified by a direct substitution to the Poisson equation,

$$\epsilon_{\parallel} \left(\frac{\partial^2}{\partial x^2} + \frac{\partial^2}{\partial y^2} \right) + \epsilon_{\perp} \frac{\partial^2}{\partial z^2} = -4\pi e \delta(\mathbf{r}, z), \quad (\text{B2})$$

where \mathbf{r} is the 2D in-plane vector. Take the distance between neighboring layers as c . A scaling to $\tilde{z} = \sqrt{\epsilon_{\parallel}/\epsilon_{\perp}}z$ in Eq. (B1) reveals that this is a Coulomb potential of a charge e in an isotropic medium of a dielectric constant $\sqrt{\epsilon_{\parallel}\epsilon_{\perp}}$ in the \mathbf{r}, \tilde{z} space.

We then follow the well-studied results of the dielectric function of layered structures in an isotropic medium [32,33]. It is given in the reciprocal space by

$$\epsilon(\mathbf{q}, \tilde{q}_z) = \sqrt{\epsilon_{\infty}^{\parallel}\epsilon_{\infty}^{\perp}} + v_q \chi \frac{\sinh(qd)}{\cosh(qd) - \cos(\tilde{q}_z d)}, \quad (\text{B3})$$

where $d = \sqrt{\epsilon_{\infty}^{\parallel}/\epsilon_{\infty}^{\perp}}c$, $\tilde{q}_z = \sqrt{\epsilon_{\infty}^{\perp}/\epsilon_{\infty}^{\parallel}}q_z$, $v_q = 2\pi e^2/q$, and χ is the response function. The effective screened Coulomb interaction is

$$V_s^{3D}(\mathbf{q}, \tilde{q}_z) = \frac{2\pi e^2}{\sqrt{\epsilon_{\infty}^{\parallel}\epsilon_{\infty}^{\perp}}q} \left[\frac{\cosh(qd) - \cos(\tilde{q}_z d)}{\sinh(qd)} + \frac{q_s}{q} \right]^{-1}, \quad (\text{B4})$$

where $q_s = 2\pi e^2 \chi / \sqrt{\epsilon_{\infty}^{\parallel}\epsilon_{\infty}^{\perp}}$.

The exciton gap equation in two dimensions of Eq. (7) would be written in three dimensions as

$$\Delta(\mathbf{k}, \tilde{k}_z) = \frac{1}{(2\pi)^2} \int_{\text{BZ}} d\mathbf{k}' \frac{c}{2\pi} \int d\tilde{k}'_z V_s^{3D}(\mathbf{k} - \mathbf{k}', \tilde{k}_z - \tilde{k}'_z) \times \frac{f(\xi_h(\mathbf{k}', \tilde{k}'_z)) - f(\xi_e(\mathbf{k}', \tilde{k}'_z))}{\xi_e(\mathbf{k}', \tilde{k}'_z) - \xi_h(\mathbf{k}', \tilde{k}'_z)} \Delta(\mathbf{k}', \tilde{k}'_z). \quad (\text{B5})$$

For cases where the z -direction dispersion can be neglected in Eq. (B5) as in strongly anisotropic materials, we may ignore the \tilde{k}_z dependence of $\Delta(\mathbf{k}, \tilde{k}_z)$ and perform the \tilde{k}'_z integral. Then, Eq. (B5) is reduced to Eq. (7), where

$$V_s(\mathbf{q}) = \frac{c}{2\pi} \int_{-\pi/d}^{\pi/d} d\tilde{q}_z V_s^{3D}(\mathbf{q}, \tilde{q}_z) = \frac{2\pi e^2}{\epsilon_{\infty}^{\parallel} q} \frac{\sinh(qd)}{\sqrt{[\cosh(qd) + \sinh(qd)\frac{q_s}{q}]^2 - 1}}, \quad (\text{B6})$$

using the relation of $\int dq_z V(q_z) = \int d\tilde{q}_z V(\tilde{q}_z)$. Note that the effective background dielectric constant $\sqrt{\epsilon_{\infty}^{\parallel}\epsilon_{\infty}^{\perp}}$ of 3D layered materials is changed to $\epsilon_{\infty}^{\parallel}$ because of the $\sqrt{\epsilon_{\infty}^{\parallel}/\epsilon_{\infty}^{\perp}}$ factor in the integrand in the q_z integral. Make expansion on the small $q_s d$ and use $\tanh(q_{\min} d) = 1.0$, where $q_{\min} = \Gamma M$ corresponds to the wavevector of the minimum gap between Γ and M points. The $q_{\min} d \gg 1$ corresponds to a weak-coupling limit which reduces the Coulomb interaction of a layered structure to that of decoupled single layers. We obtain

$$V_s(\mathbf{q}) = \frac{2\pi e^2}{\epsilon_{\infty}^{\parallel}} \frac{1}{q + q_s}. \quad (\text{B7})$$

This shows that the effective background dielectric constant in the 2D modeling of the screened Coulomb interaction is given

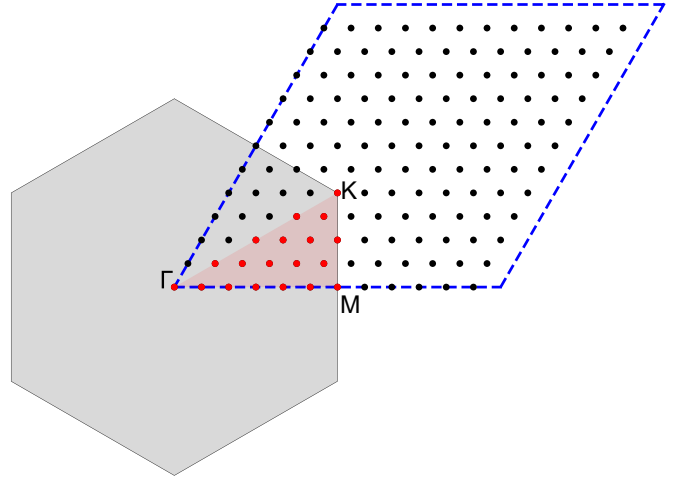


FIG. 5. The gray hexagonal area represents 1st BZ of TiSe_2 . It can be converted into the blue dash rhombus of the same area. The red and black dots in the blue dashed rhombus are the selected k points for FFT. The red dots are the k points in the irreducible BZ (pale red triangle) for T_c calculations.

by the in-plane component of the background dielectric tensor of 3D layered materials.

APPENDIX C: CALCULATION OF T_c

There are a few characteristics of the electronic structure of candidate materials relevant for the exciton condensation: (a) direct or indirectness of the band gap, (b) the normal gap size E_g , (c) the number of electron bands and hole bands, (d) mass asymmetry, the ratio of hole to electron masses $\beta = m_h/m_e$, and (e) the background dielectric constant. All these material-specific electronic structures were incorporated in the calculations of the critical temperature T_c of the exciton condensation.

To calculate T_c , the linearized gap equation was written in a matrix form by discretizing the wavevector \mathbf{k} within first BZ as given in Eq. (8) in the main text. The discretization of the wavevector \mathbf{k} was taken as the 48×48 points as shown in Fig. 5. For calculation efficiency, \mathbf{k}_i points were selected within the irreducible BZ (red dots in red area) with the weight of each point properly taken into account. This produces $\sim 1/12$ times smaller matrix size to diagonalize. Equation (8) is just an eigenvalue problem with the eigenvalue set to 1. For temperatures above the critical temperature T_c all the eigenvalues are smaller than 1. T_c is given by the temperature where the largest eigenvalue of the matrix M of Eq. (8) becomes 1. This sets up a route to determine the EI critical temperature T_c microscopically with the electronic structure properties like ϵ_{∞} and E_g and with no fitting parameters.

Figure 6(a) shows the critical temperature T_c of EI in two dimensions for four different cases of the characteristics. The calculated EI phase on the negative E_g region strongly depends on the material parameters, while it is more robust on the positive E_g side. All of the characteristic configurations affect the suppression of the EI phase on the negative E_g region. In particular, the EI phase on the negative E_g region is completely suppressed for indirect gap configurations or

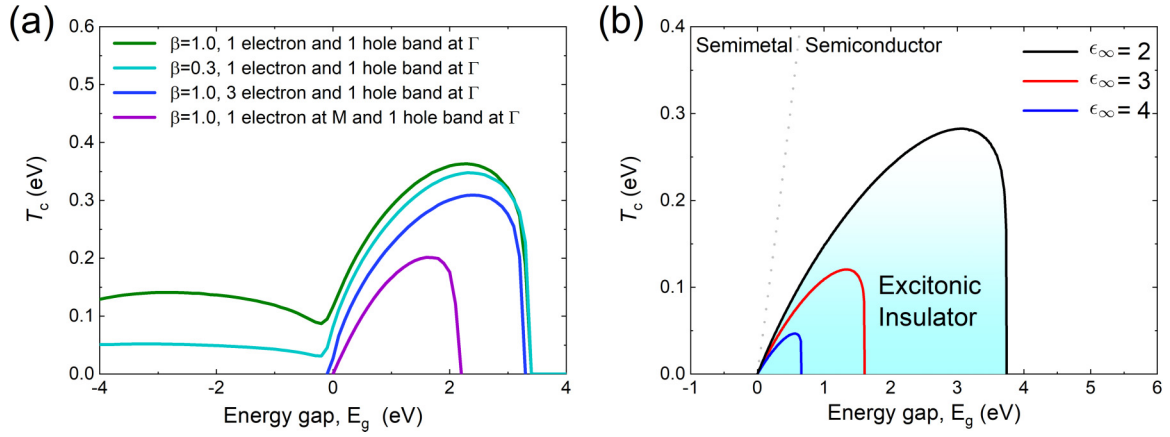


FIG. 6. (a) The critical temperature T_c of excitonic instability as a function of the energy gap for four different characteristic configurations of electronic structure. (b) T_c vs E_g for TiSe₂ for different choices of the background dielectric constant ϵ_∞ .

the number of conduction bands being greater than 1. The exciton condensation is not expected in the semimetallic cases for TiSe₂. Figure 6(b) shows T_c vs E_g for TiSe₂ for different choices of the background dielectric constant $\epsilon_\infty = 2, 3$, and 4. T_c is suppressed as E_g is increased.

The E_g where $T_c \rightarrow 0$ on the positive E_g side is the exciton binding energy E_X . Figure 6 shows that the E_X is reduced in the indirect gap cases as given in Eq. (9) in the main text. Consider the gap equation of Eq. (7). Take the $T \rightarrow 0$ limit and determine the positive E_g that satisfies the equation. From Eq. (A19)

$$\begin{aligned} \xi_e - \xi_h &= E_g + \left(\frac{\hbar^2}{2m_e} + \frac{\hbar^2}{2m_h} \right) k^2 + \frac{\hbar^2}{2m_e} (\overline{\Gamma M}^2 - 2k\overline{\Gamma M}) \\ &= E_g + \frac{\hbar^2 \overline{\Gamma M}^2}{2M} + \frac{\hbar^2}{2m_r} \left(k - \frac{m_r}{m_e} \overline{\Gamma M} \right)^2, \end{aligned} \quad (C1)$$

where M and m_r are the total and reduced masses of an electron and a hole of an exciton,

$$M = m_e + m_h, \quad \frac{1}{m_r} = \frac{1}{m_e} + \frac{1}{m_h}. \quad (C2)$$

For a rough estimate of E_X , we neglect the k dependence of the order parameter for simplicity and extend the range of integration of Eq. (7) to the entire wavevector space to obtain

$$\begin{aligned} 1 &= \int d^2k \frac{e^2}{2\pi\epsilon_\infty k} \frac{1}{E_g + \frac{\hbar^2 \overline{\Gamma M}^2}{2M} + \frac{\hbar^2}{2m_r} k^2} \\ &= \frac{\alpha}{\epsilon_\infty} \frac{2m_r c \pi}{\hbar} \frac{1}{\sqrt{\frac{2m_r}{\hbar^2} \left(E_g + \frac{\hbar^2 \overline{\Gamma M}^2}{2M} \right)}}. \end{aligned} \quad (C3)$$

Then, the exciton binding energy is given by

$$E_X \approx 2m_r c^2 \left(\frac{\alpha}{\epsilon_\infty} \right)^2 - \frac{\hbar^2 \overline{\Gamma M}^2}{2M}, \quad (C4)$$

as given in Eq. (9) in the main text. The first term on the right-hand side is the well-known binding energy of a direct exciton in two dimensions. For T_c of layered structures, E_X is

modified to

$$E_X \approx 2m_r c^2 \frac{\alpha^2}{\epsilon_\infty \epsilon_\infty^\perp} - \frac{\hbar^2 \overline{\Gamma L}^2}{2M}, \quad (C5)$$

where E_X is reduced by the indirectness of the gap. A slight increase of ϵ_∞ or a decrease of M such that the first term becomes smaller than the second one on the right-hand side of Eq. (C4) then completely suppresses an EI phase in candidate materials. Figure 7 shows a contour plot of excitonic T_c of TiSe₂ in the ϵ_∞ - E_g plane. For example, for $\epsilon_\infty \approx 4.0$, $E_X \approx 0.6$ eV, and for $\epsilon_\infty \gtrsim 4.5$ the EI phase is completely suppressed because $E_g \gtrsim E_X$ as can be seen from Fig. 7.

Figure 8 shows the calculated critical temperature T_c as a function of E_g from the 3D gap equation [Eq. (B5)] with the screened Coulomb interaction of layered structures [Eq. (B4)] in comparison with the 2D results from Fig. 2(a). The E_g refers to the minimum gap between the electron and hole bands and corresponds to the gap between Γ and L in three dimensions (M in two dimensions). The k_z dispersion, therefore, widens

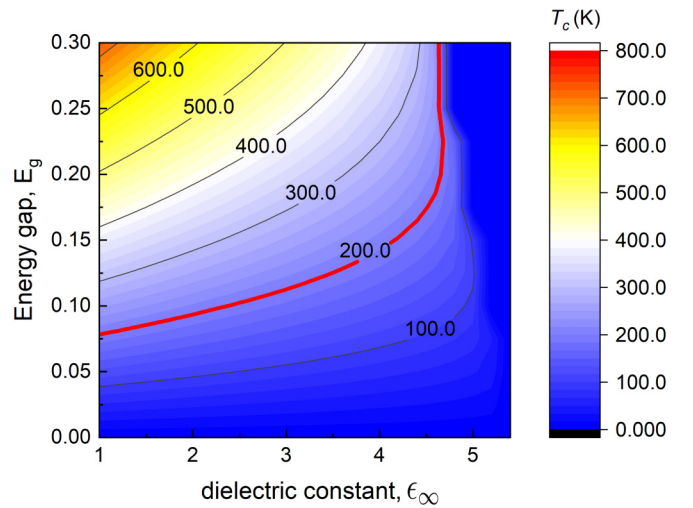


FIG. 7. Contour plot of the exciton critical temperature for TiSe₂ in the plane of the background dielectric constant ϵ_∞ and the normal gap E_g . The red line represents the region corresponding to $T_c = 200$ K.

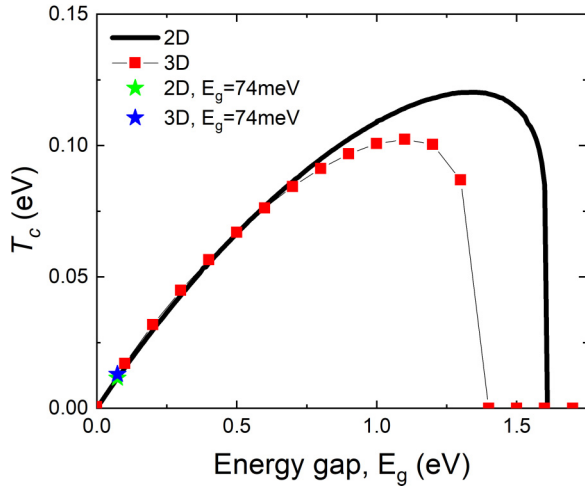


FIG. 8. The exciton critical temperature for TiSe_2 as a function of the normal gap E_g from 3D gap equation.

the gap between the electron and hole bands on average which around 74 meV negates weakening of screened Coulomb interaction and leads to an increase of T_c . We adapted the parametrization for the k_z dispersion as given by Monney *et al.* [11], adding

$$t_e \cos(\pi k_z / \overline{\Gamma A}), \quad t_h \cos(\pi k_z / \overline{\Gamma A}), \quad (\text{C6})$$

to the electron and hole dispersions, respectively, with $t_e = 30 \pm 2.5$ meV and $t_h = 60 \pm 5$ meV. For $\epsilon_\infty^\perp = 3.25$ as determined from the *ab initio* calculation as explained in Appendix D and $\epsilon_\infty^\parallel = 3.0$ the same as the 2D calculations, T_c increased to 150 K around $E_g \approx 74$ meV as shown in Fig. 8. Another change is that the exciton binding energy E_X decreased to around 1.3 eV in three dimensions (1.6 in two dimensions). This is as anticipated because the first term of Eq. (C5) in comparison with Eq. (C4) decreases and the second term increases in three dimensions.

APPENDIX D: DETERMINATION OF ϵ_∞ OF $1T\text{-TiSe}_2$

We determined the background dielectric constant ϵ_∞ by combining the measured reflectance spectrum below 6.2 eV [34], and the measured electron energy loss spectroscopy spectrum up to 30 eV [35]. We also used the *ab initio* calculated real and imaginary parts of the dielectric functions in a published paper [36] to check reliability of the determined value from the experiments. They are in good agreement with each other as we discuss below.

The reflectance spectrum $R(\omega)$ for the normal incidence is given in terms of the complex dielectric constant $\tilde{\epsilon}(\omega) \equiv \epsilon_1(\omega) + i\epsilon_2(\omega)$ by

$$R(\omega) = \left| \frac{1 - \sqrt{\tilde{\epsilon}(\omega)}}{1 + \sqrt{\tilde{\epsilon}(\omega)}} \right|^2. \quad (\text{D1})$$

The separate reflectance spectra at 300 K are shown in Fig. 9, and the combined reflectance spectrum is shown in the inset. We performed the Kramers-Kronig (KK) analysis [37] to get the optical conductivity from the combined reflectance spectrum. The optical conductivity is shown in Fig. 10.

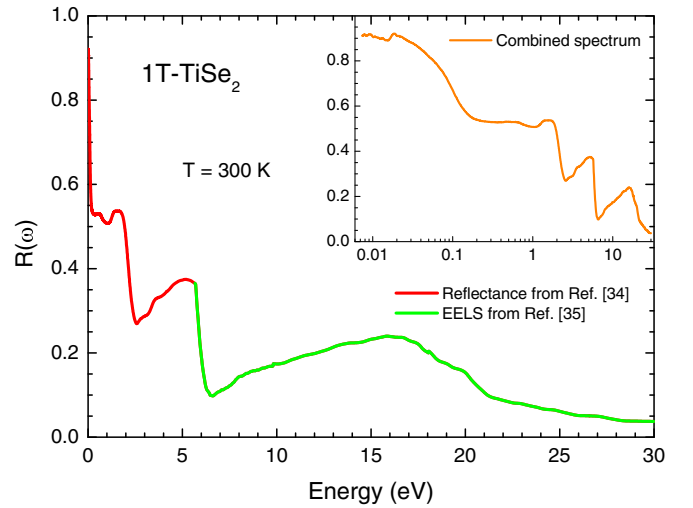


FIG. 9. Separate reflectance spectra of $1T\text{-TiSe}_2$ at 300 K obtained from the optical spectroscopy [34] and the EELS study [35]. In the inset we show the combined reflectance.

The largest interband optical transition between the electron and hole bands of Eqs. (A19) considered in the present calculations is about 6.5 eV within the first BZ. The excitations above 6.5 eV then contribute to the background dielectric constant ϵ_∞ . We used the method introduced in [38] to estimate ϵ_∞ from the optical conductivity above 6.5 eV. We obtain the imaginary part of the optical conductivity above 6.5 eV using the Kramers-Kronig relation [37] between the real and imaginary parts of the optical conductivity. Also using the relation between the imaginary part of the optical conductivity and the real part of the dielectric function, we obtain the background dielectric constant as

$$\epsilon_\infty \equiv \lim_{\omega \rightarrow 0} \epsilon_1^H(\omega),$$

$$\epsilon_1^H(\omega) = 1 - \frac{4\pi}{\omega} \sigma_2^H(\omega). \quad (\text{D2})$$

$\epsilon_\infty = 3.0$ as can be seen in Fig. 11.

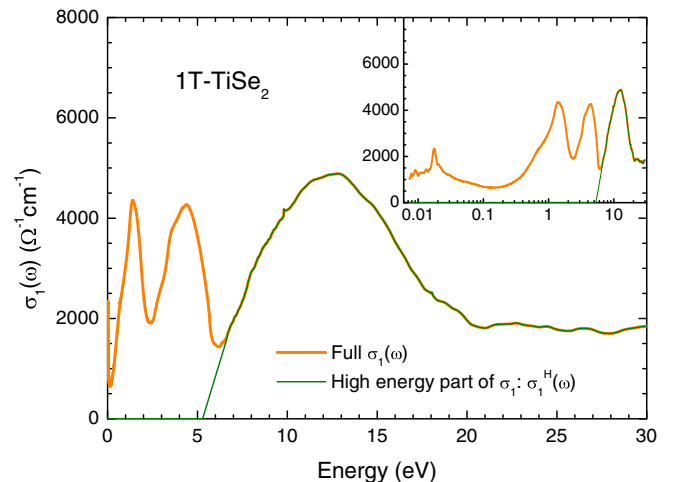


FIG. 10. The optical conductivity: the full conductivity (orange line) and a high-energy part above 6.5 eV (olive line).

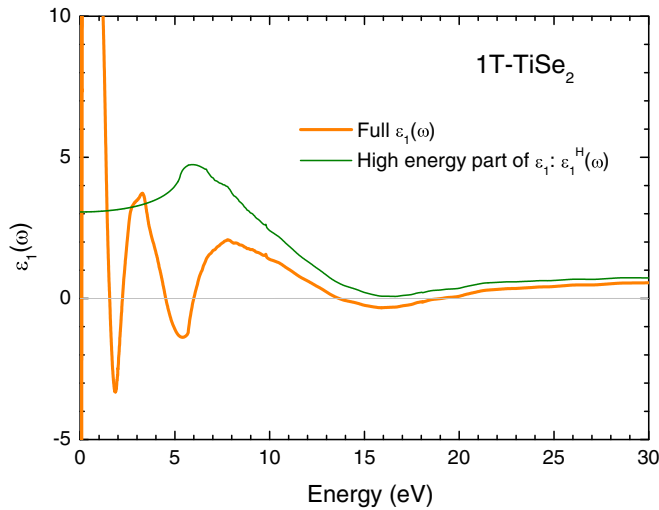


FIG. 11. The dielectric function $\epsilon_1(\omega)$ of 1T-TiSe₂ obtained from the KK analysis and the high-energy dielectric function, $\epsilon_1^H(\omega)$.

The ϵ_∞ , having been determined by the contributions from high-energy excitations above the cutoff of 6.5 eV, should be temperature independent. To demonstrate this explicitly, we used the 10 K experimental data to determine ϵ_∞ at $T = 10$ K. As can be seen from Fig. 12 the conductivities at 10 K (blue curve) and 300 K (red) merge above around 1 eV. The ϵ_∞ is determined from the high-energy part (green curve) where the two different T data overlap exactly. This explicitly shows that the background dielectric constant ϵ_∞ is temperature independent as expected.

Since the exciton instability is rather sensitive on the ϵ_∞ value as can be seen, for example, from Eq. (9), we checked the reliability of the determined value of $\epsilon_\infty = 3.0$. We proceed exactly the same now with the *ab initio* evaluated real and imaginary parts of the dielectric functions $\epsilon_1(\omega)$ and $\epsilon_2(\omega)$ for the in-plane electric field ($\mathbf{E} \perp \hat{z}$) in a published

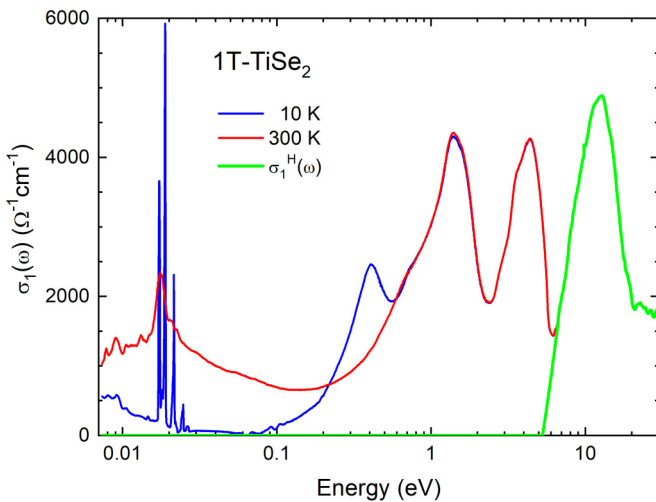


FIG. 12. The conductivity $\sigma_1(\omega)$ and the high-energy part of the conductivity $\sigma_1^H(\omega)$ for temperatures 10 and 300 K. The $\sigma_1^H(\omega)$ for the two temperatures overlap exactly and, consequently, the background dielectric constant ϵ_∞ is temperature independent.

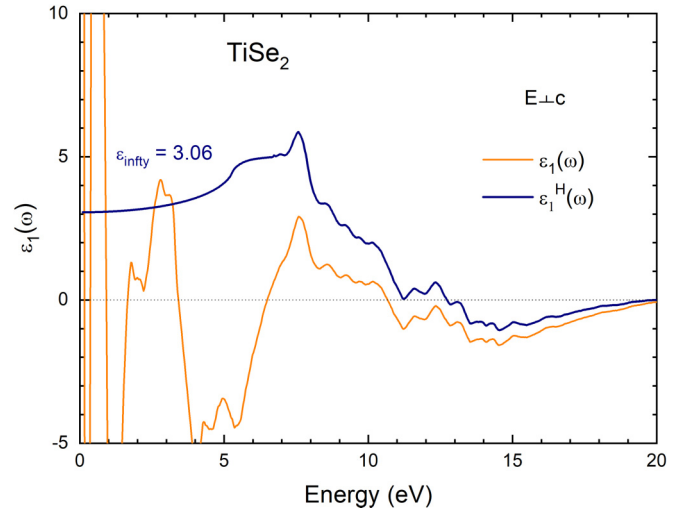


FIG. 13. The dielectric function $\epsilon_1(\omega)$ and the high-energy part of the dielectric function $\epsilon_1^H(\omega)$ for the electric field parallel to the layers.

paper [36]. We obtained $\epsilon_\infty^\parallel = 3.06$ as can be seen in Fig. 13 in good agreement with the $\epsilon_\infty^\parallel = 3.0$ from the combined data of reflectance and EELS.

We also determined ϵ_∞^\perp from the *ab initio* calculations for the out-of-plane electric field [36]. We obtained $\epsilon_\infty^\perp = 3.25$ as can be seen in Fig. 14. Then, the 3D effective background dielectric constant is $\sqrt{\epsilon_\infty^\parallel \epsilon_\infty^\perp} = 3.15$.

APPENDIX E: COMPARISON WITH STS AND STM EXPERIMENTS

In the low-temperature limit, we need to solve the full gap equation of Eq. (1) in the main text. The \mathbf{k}' summation was performed using the fast Fourier transform (FFT) between the momentum and real space for accuracy and efficiency using

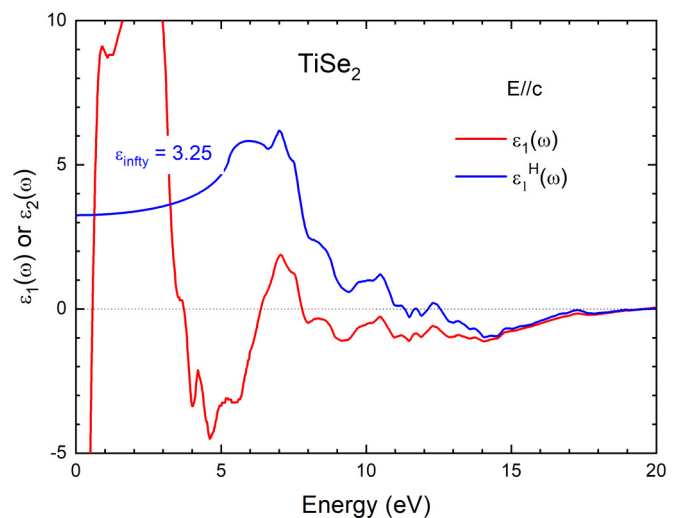


FIG. 14. The full dielectric function and the high-energy part of the dielectric function for the electric field perpendicular to the layers.

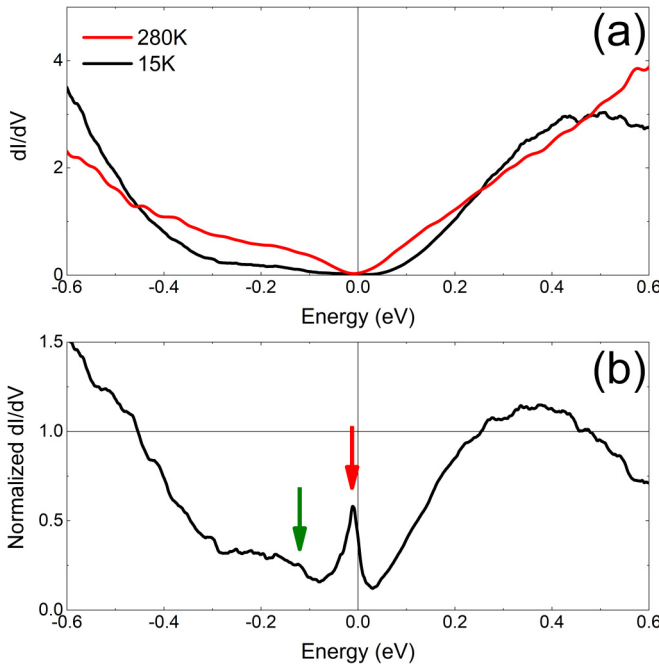


FIG. 15. (a) The dI/dV of TiSe_2 at 280 K (red) and 15 K (black) from Kolekar *et al.* [27]. (b) Normalized dI/dV .

the convolution relation

$$\sum_{\mathbf{k}} e^{i\mathbf{k}\cdot\mathbf{r}} \sum_{\mathbf{k}'} F(\mathbf{k}' - \mathbf{k})G(\mathbf{k}') = F(\mathbf{r})G(\mathbf{r}). \quad (\text{E1})$$

Then, Eq. (1) may be transformed to the real space as

$$\Delta_i(\mathbf{r}) = - \int_{-\infty}^{\infty} d\omega A_{\Delta_i}(\mathbf{r}, \omega) f(\omega) V_s(\mathbf{r}). \quad (\text{E2})$$

The screened Coulomb interaction and the spectral function in the real space, $V_s(\mathbf{r})$ and $A(\mathbf{r}, \omega)$, respectively, were also obtained by performing FFT. The k points in the 2D hexagonal

lattice (gray area in Fig. 5) are not suitable for performing FFT, so a 2D rhombus lattice (dashed line in the figure) of the same size was considered. The k points were selected evenly spaced within the 2D rhombus lattice (red and black dots in the figure). The selected k points naturally include the periodicity of the 2D hexagonal lattice. At this time, in order to fully consider the information of the 2D hexagonal lattice, the number of k points on one side was set to an integer multiple of 6. Here we choose 48×48 k points as shown in Fig. 5. Since the rhombus is an inclined rectangle, the selected k points can be applied to the conventional 2D FFT algorithm.

The gap equation (E2) was solved self-consistently via numerical iterations. The $\Delta_i(\mathbf{k})$ ($i = 1, 2, 3$) are all coupled in the full gap equation. They were obtained simultaneously from iterations without making symmetry operations among them. The obtained $\Delta_i(\mathbf{k})$ were shown in Fig. 3. With thus determined $\Delta_i(\mathbf{k})$ the spectroscopic features were calculated as explained in main text. The semiconducting DOS of our model TiSe_2 [Fig. 4(c), red solid line] gets enlarged in the EI phase [Fig. 4(c), black solid line]. Some detailed structures, split weak coherence peaks, and steplike structures are as we may expect from the ARPES intensity.

These features may be revealed more clearly in the normalized DOS as shown in Fig. 4(d) in the main text. A remarkable structure in the normalized DOS from calculations is the zero-bias peak, which is caused by a semiconducting normal state. The corresponding DOS plots from STS experiments by Kolekar *et al.* [27] are shown for both normal [Fig. 15(a), red solid line] and CDW phases [Fig. 15(a), black solid line], and the normalized DOS in Fig. 15(b). It is not straightforward to determine the gap size from experiments because there is no strong coherence peak. But this weak coherence peak is consistent with calculations. A steplike structure around -0.1 to -0.2 eV can be compared with calculations, although the energy scale is not clear. Interestingly, the zero-bias peak also appears in normalized DOS from experiments. For more systematic comparison, one may need a systematic measurement and analysis of STS and/or STM for above and below T_c .

- [1] N. F. Mott, The transition to the metallic state, *Philos. Mag.* **6**, 287 (1961).
- [2] D. Snoke, Spontaneous Bose coherence of excitons and polaritons, *Science* **298**, 1368 (2002).
- [3] D. Jérôme, T. M. Rice, and W. Kohn, Excitonic insulator, *Phys. Rev.* **158**, 462 (1967).
- [4] W. Kohn and D. Sherrington, Two kinds of bosons and Bose condensates, *Rev. Mod. Phys.* **42**, 1 (1970).
- [5] B. I. Halperin and T. M. Rice, Possible anomalies at a semimetal-semiconductor transition, *Rev. Mod. Phys.* **40**, 755 (1968).
- [6] J. P. Eisenstein and A. H. MacDonald, Bose-Einstein condensation of excitons in bilayer electron systems, *Nature* **432**, 691 (2004).
- [7] X. Liu, K. Watanabe, T. Taniguchi, B. I. Halperin, and P. Kim, Quantum Hall drag of exciton condensate in graphene, *Nat. Phys.* **13**, 746 (2017).
- [8] J. I. A. Li, T. Taniguchi, K. Watanabe, J. Hone, and C. R. Dean, Excitonic superfluid phase in double bilayer graphene, *Nat. Phys.* **13**, 751 (2017).
- [9] F. J. Di Salvo, D. E. Moncton, and J. V. Waszczak, Electronic properties and superlattice formation in the semimetal TiSe_2 , *Phys. Rev. B* **14**, 4321 (1976).
- [10] M. M. Traum, G. Margaritondo, N. V. Smith, J. E. Rowe, and F. J. Di Salvo, TiSe_2 : Semiconductor, semimetal, or excitonic insulator, *Phys. Rev. B* **17**, 1836 (1978).
- [11] C. Monney, H. Cercellier, F. Clerc, C. Battaglia, E. F. Schwier, C. Didiot, M. G. Garnier, H. Beck, P. Aebi, H. Berger, L. Forró, and L. Patthey, Spontaneous exciton condensation in $1T$ - TiSe_2 : BCS-like approach, *Phys. Rev. B* **79**, 045116 (2009).
- [12] H. Cercellier, C. Monney, F. Clerc, C. Battaglia, L. Despont, M. G. Garnier, H. Beck, P. Aebi, L. Patthey, H. Berger, and L. Forró, Evidence for an Excitonic Insulator Phase in $1T$ - TiSe_2 , *Phys. Rev. Lett.* **99**, 146403 (2007).
- [13] G. Grüner, *Density Waves in Solids* (Perseus Books, New York, 2000).
- [14] K. Rossnagel, L. Kipp, and M. Skibowski, Charge-density-wave phase transition in $1T$ - TiSe_2 : Excitonic insulator versus band-type Jahn-Teller mechanism, *Phys. Rev. B* **65**, 235101 (2002).

- [15] A. Kogar, M. S. Rak, S. Vig, A. A. Husain, F. Flicker, Y. Il Joe, Luc Venema, G. J. MacDougall, T. C. Chiang, E. Fradkin, J. van Wezel, and P. Abbamonte, Signatures of exciton condensation in a transition metal dichalcogenide, *Science* **358**, 1314 (2017).
- [16] M. Porer, U. Leierseder, J.-M. Ménard, H. Dachraoui, L. Mouchliadis, I. E. Perakis, U. Heinzmann, J. Demsar, K. Rossnagel, and R. Huber, Non-thermal separation of electronic and structural orders in a persisting charge density wave, *Nat. Mater.* **13**, 857 (2014).
- [17] F. X. Bronold and H. Fehske, Possibility of an excitonic insulator at the semiconductor-semimetal transition, *Phys. Rev. B* **74**, 165107 (2006).
- [18] M. D. Watson, O. J. Clark, F. Mazzola, I. Marković, V. Sunko, T. K. Kim, K. Rossnagel, and P. D. C. King, Orbital- and k_z -Selective Hybridization of Se $4p$ and Ti $3d$ States in the Charge Density Wave Phase of TiSe_2 , *Phys. Rev. Lett.* **122**, 076404 (2019).
- [19] E. Morosan, H. W. Zandbergen, B. S. Dennis, J. W. G. Bos, Y. Onose, T. Klimczuk, A. P. Ramirez, N. P. Ong, and R. J. Cava, Superconductivity in Cu_xTiSe_2 , *Nat. Phys.* **2**, 544 (2006).
- [20] P. Chen, Y. H. Chan, X. Y. Fang, Y. Zhang, M. Y. Chou, S. K. Mo, Z. Hussain, A. V. Fedorov, and T. C. Chiang, Charge density wave transition in single-layer titanium diselenide, *Nat. Commun.* **6**, 8943 (2015).
- [21] P. Goli, J. Khan, D. Wickramaratne, R. K. Lake, and A. A. Balandin, Charge density waves in exfoliated films of van der Waals materials: Evolution of Raman spectrum in TiSe_2 , *Nano Lett.* **12**, 5941 (2012).
- [22] A. Chernikov, T. C. Berkelbach, H. M. Hill, A. Rigosi, Y. Li, O. B. Aslan, D. R. Reichman, M. S. Hybertsen, and T. F. Heinz, Exciton Binding Energy and Nonhydrogenic Rydberg Series in Monolayer WS_2 , *Phys. Rev. Lett.* **113**, 076802 (2014).
- [23] Y. F. Lu, H. Kono, T. I. Larkin, A. W. Rost, T. Takayama, A. V. Boris, B. Keimer, and H. Takagi, Zero-gap semiconductor to excitonic insulator transition in Ta_2NiSe_5 , *Nat. Commun.* **8**, 14408 (2017).
- [24] A. F. Kusmartseva, B. Sipos, H. Berger, L. Forró, and E. Tutiš, Pressure Induced Superconductivity in Pristine $1T$ - TiSe_2 , *Phys. Rev. Lett.* **103**, 236401 (2009).
- [25] T. Jaouen, M. Rumo, B. Hildebrand, M. L. Mottas, C. W. Nicholson, G. Kremer, B. Salzmann, F. Vanini, C. Barreteau, E. Giannini, H. Beck, P. Aebi, and C. Monney, Unveiling the semimetallic nature of $1T$ - TiSe_2 by doping its charge density wave, [arXiv:1911.06053](https://arxiv.org/abs/1911.06053).
- [26] T. E. Kidd, T. Miller, M. Y. Chou, and T.-C. Chiang, Electron-Hole Coupling and the Charge Density Wave Transition in TiSe_2 , *Phys. Rev. Lett.* **88**, 226402 (2002).
- [27] S. Kolekar, M. Bonilla, Y. Ma, H. C. Diaz, and M. Batzill, Layer- and substrate-dependent charge density wave criticality in $1T$ - TiSe_2 , *2D Mater.* **5**, 015006 (2018).
- [28] A. M. Novello, B. Hildebrand, A. Scarfato, C. Didiot, G. Monney, A. Ubaldini, H. Berger, D. R. Bowler, P. Aebi, and Ch. Renner, Scanning tunneling microscopy of the charge density wave in $1T$ - TiSe_2 in the presence of single atom defects, *Phys. Rev. B* **92**, 081101(R) (2015).
- [29] D. J. Campbell, C. Eckberg, P. Y. Zavalij, H.-H. Kung, E. Razzoli, M. Michiardi, C. Jozwiak, A. Bostwick, E. Rotenberg, A. Damascelli, and J. Paglione, Intrinsic insulating ground state in transition metal dichalcogenide TiSe_2 , *Phys. Rev. Mater.* **3**, 053402 (2019).
- [30] J. M. Moya, C.-L. Huang, J. Choe, G. Costin, M. S. Foster, and E. Morosan, Effect of synthesis conditions on the electrical resistivity of TiSe_2 , *Phys. Rev. Mater.* **3**, 084005 (2019).
- [31] C. Chen, B. Singh, H. Lin, and V. M. Pereira, Reproduction of the Charge Density Wave Phase Diagram in $1T$ - TiSe_2 Exposes its Excitonic Character, *Phys. Rev. Lett.* **121**, 226602 (2018).
- [32] P. B. Visscher and L. M. Falicov, Dielectric screening in a layered electron gas, *Phys. Rev. B* **3**, 2541 (1971).
- [33] K. W. K. Shung, Dielectric function and plasmon structure of stage-1 intercalated graphite, *Phys. Rev. B* **34**, 979 (1986).
- [34] G. Li, W. Z. Hu, D. Qian, D. Hsieh, M. Z. Hasan, E. Morosan, R. J. Cava, and N. L. Wang, Semimetal-to-Semimetal Charge Density Wave Transition in $1T$ - TiSe_2 , *Phys. Rev. Lett.* **99**, 027404 (2007).
- [35] G.-J. Shu, Y. Zhou, M.-Y. Kao, C. J. Klingshirn, M. R. S. Huang, Y.-L. Huang, Y. Liang, W. C. H. Kuo, and S.-C. Liou, Investigation of the π plasmon and plasmon-exciton coupling in titanium diselenide (TiSe_2) by momentum-resolved electron energy loss spectroscopy, *Appl. Phys. Lett.* **114**, 202103 (2019).
- [36] A. Leventi-Peetz, E. E. Krasovskii, and W. Schattke, Dielectric function and local-field effects of TiSe_2 , *Phys. Rev. B* **51**, 17965 (1995).
- [37] F. Wooten, *Optical Properties of Solids* (Academic Press, New York, 1972).
- [38] J. Hwang, T. Timusk, and G. D. Gu, Doping dependent optical properties of $\text{Bi}_2\text{Sr}_2\text{CaCu}_2\text{O}_{8+\delta}$, *J. Phys.: Condens. Matter* **19**, 125208 (2007).